Ultrafast (≈10 GHz) mid-IR modulator based on ultrafast electrical switching of the light–matter coupling ⊕✓

Mario Malerba ✉ ⓘ ; Stefano Pirotta; Guy Aubin ⓘ ; L. Lucia ⓘ ; M. Jeannin ⓘ ; J.-M. Manceau ⓘ ; A. Bousseksou ⓘ ; Q. Lin; J.-F. Lampin ⓘ ; E. Peytavit ⓘ ; S. Barbieri ⓘ ; L. H. Li ⓘ ; A. G. Davies ⓘ ; E. H. Linfield ⓘ ; Raffaele Colombelli ✉ ⓘ

Check for updates

View Online   Export Citation

Applied Physics Letters

AIP Publishing

Ultrafast (≈10 GHz) mid-IR modulator based on ultrafast electrical switching of the light–matter coupling EP

Mario Malerba,[1,a),b)] iD Stefano Pirotta,[1] Guy Aubin,[1] iD L. Lucia,[1] iD M. Jeannin,[1] iD J.-M. Manceau,[1] iD
A. Bousseksou,[1] iD Q. Lin,[2] J.-F. Lampin,[2] E. Peytavit,[2] iD S. Barbieri,[2] iD L. H. Li,[3] iD A. G. Davies,[3] iD E. H. Linfield,[3] iD
and Raffaele Colombelli[1,b)] iD

AFFILIATIONS

[1]Centre de Nanosciences et de Nanotechnologies, CNRS UMR 9001, Université Paris Saclay, 10 Boulevard Thomas Gobert, 91120 Palaiseau, France

[2]Institute of Electronics, Microelectronics and Nanotechnology, CNRS, University Lille, University Polytechnique Hauts-de-France, UMR 8520, F-59000 Lille, France

[3]School of Electronic and Electrical Engineering, University of Leeds, Leeds LS2 9JT, United Kingdom

a)**Present address**: Istituto Nazionale di Ricerca Metrologica (INRIM), Strada delle Cacce 91, 10135 Torino, Italy
b)**Authors to whom correspondence should be addressed**: m.malerba@inrim.it and raffaele.colombelli@universite-paris-saclay.fr

ABSTRACT

We demonstrate a free-space amplitude modulator for mid-infrared radiation ($\lambda \approx 9.6\,\mu m$) that operates at room temperature up to at least 20 GHz (above the −3 dB cutoff frequency measured at 8.2 GHz). The device relies on the ultrafast transition between weak- and strong-coupling regimes induced by the variation of the applied bias voltage. Such transition induces a modulation of the device reflectivity. It is made of a semiconductor heterostructure enclosed in a judiciously designed array of metal–metal optical resonators, that—all-together—behave as an electrically tunable surface. At negative bias, it operates in the weak light–matter coupling regime. Upon application of an appropriate positive bias, the quantum wells populate with electrons, and the device transitions to the strong-coupling regime. The modulator transmission remains linear with input radio frequency power in the 0–9 dBm range. The increase in optical powers up to 25 mW exhibit a weak beginning of saturation a little bit below.

Published under an exclusive license by AIP Publishing. https://doi.org/10.1063/5.0213965

Electrically reconfigurable surfaces are artificial components whose optical properties, in reflection/absorption, can be addressed electrically.[1–3] In particular, surfaces whose complex reflectivity (real/imaginary parts of the S11 parameter, in electronic scattering terms) is electrically tunable are particularly useful as amplitude or phase modulators.[4–7] In the mid-infrared (IR) ($3\,\mu m < \lambda < 30\,\mu m$), these functionalities are useful for applications such as laser amplitude/frequency stabilization,[8] coherent detection, spectroscopy and sensing, mode-locking, and optical communications.[9] However, the ultrafast (10–40 GHz) modulation of mid-IR radiation has been for a long time a largely under-developed functionality.[10–12] Recently, advances have been proposed, in semi-guided/guided architectures, on III–V[13] and on SiGe platforms.[14] In the former case, an optical 10 Gbit/s free-space transmission at 9 μm has been demonstrated despite a 3 dB cutoff at 3 GHz of the full system. In the latter case, operation was reported up to ≈1.5 GHz.

An alternative is to implement electrically reconfigurable surfaces for the mid-IR, where they are not as developed as in the visible/telecom spectral regions or as in the radio frequency (RF) domain.[17] This is the path that we have recently proposed in a proof-of-concept demonstration.[18] One of the advantages of this approach is that such devices would be immediately deployable in existing mid-IR setups that—in the vast majority—operate with free-space propagating beams.

The operating principle is described in Figs. 1(a) and 1(b). A judiciously designed semiconductor heterostructure active region (AR), whose details are given in the supplementary material, is embedded in an array of metal-insulator-metal (MIM) optical resonators that are electrically connected so that a bias can be applied [panel (a), sketch]. At negative bias, the active quantum well (QW) is depleted, and the AR does not absorb: only the cavity absorption peak appears in
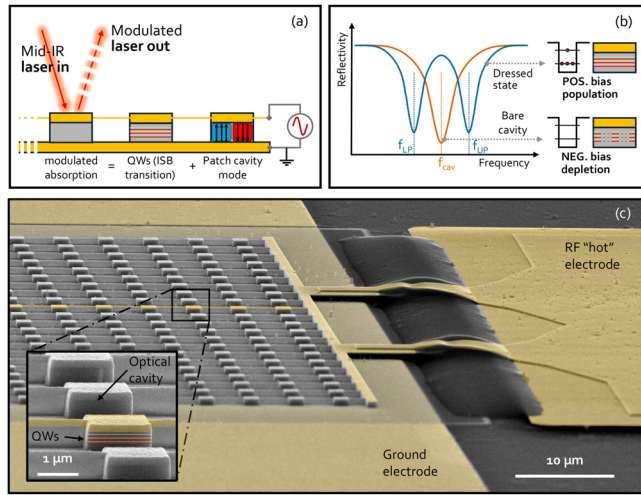
FIG. 1. (a) Scheme of the modulator architecture: the active region is embedded in metal–metal cavities that are electrically connected. The amplitude of the optical reflected beam is modulated by the application of an external RF signal. (b) Intuitive view of the modulator operating principle in an ideal configuration. (c) SEM images of a typical fabricated device.

reflectivity [Fig. 1(b), orange line] at the energy $\hbar\omega_{cav}$. The application of a positive bias populates the QWs and activates the AR absorption at $\hbar\omega_{12}$ (see Fig. 2): since the device is designed to operate in strong coupling, the reflectivity features two polaritonic resonances at energies $\hbar\omega_{LP,UP} = \hbar\omega_{cav} \pm \hbar\Omega_{Rabi}$, as sketched in Fig. 1(b), blue line. $\hbar\omega_{LP,UP}$ are the energies of the lower (upper) polariton modes, respectively. $\hbar\omega_{cav}$ is the energy of the cavity mode, which depends on the cavity geometry. We operate on the fundamental TM_{10} cavity mode, as defined in Ref. 19. In addition, $\hbar\Omega_{Rabi}$ is the Rabi energy, that gauges the strength of the light–matter coupling. If a laser beam is shone on the device surface, and the bias is properly modulated [see sketch in

Fig. 1(a)], the reflectivity change induces a corresponding amplitude modulation of the laser beam. The effect is maximum at photon energies around $\hbar\omega_{LP,UP}$ and $\hbar\omega_{cav}$.

In this Letter, we demonstrate that this approach permits to implement a free-space amplitude modulator for mid-infrared radiation ($\lambda \approx 9.6\,\mu m$) that operates at room temperature up to at least 20 GHz, with an optical -3 dB cutoff frequency around 10 GHz.

The InGaAs/AlInAs semiconductor heterostructure was grown by molecular beam epitaxy lattice-matched on a low-doped InP substrate. It is composed of eight periods of a double QW structure separated by 14-nm-thick AlInAs barriers. Each double-QW is composed of a 9.3-nm-thick active InGaAs well, separated by a 3.1-nm-thick AlInAs barrier from a larger 16-nm-thick InGaAs QW. The latter well is delta doped in the center with silicon to a nominal level of 1.2 $\times$ 10^{12} cm^{-2}. The AR is preceded and capped by 40 and 10 nm InGaAs, respectively. The structure is inspired from a GaAs/AlGaAs design reported in Ref. 20, and details are reported in the supplementary material.

At negative bias, the electronic band structure of a period of the AR is reported in Fig. 2(a). The active transition is $1 \rightarrow 2$, designed at $\lambda = 8.85\,\mu m$, but the active QW (the narrower QW in the figure) is depleted, as electrons are localized in the right well. As a consequence, there is no absorption: once the AR is inserted in a MIM resonator, only the cavity dip appears in reflectivity.

This behavior persists up to 0 V, where only a small fraction of the electrons populates state $|1\rangle$. As a consequence, the device operates in weak coupling, and only one dip is apparent in reflectivity.

When a positive bias is applied, level $|0\rangle$ is progressively brought in alignment with level $|1\rangle$: carriers delocalize via tunneling, and the $1 \rightarrow 2$ absorption increases. The quantity that gauges this process is the plasma frequency $\omega_{pl} = \sqrt{\frac{f_{12}n_{2D}e^2}{\epsilon_{InGaAs}\epsilon_0 m^* L_{QW}}}$, where f_{12} is the oscillator strength of the active transition [the $1 \rightarrow 2$ transition in Fig. 2(a)]; n_{2D} is the surface electronic density difference between subbands 1 and 2; m^* is the active QW effective mass [the narrower QW in Fig. 2(a); the material is InGaAs]; L_{QW} is the active QW width; ϵ_{InGaAs} is the
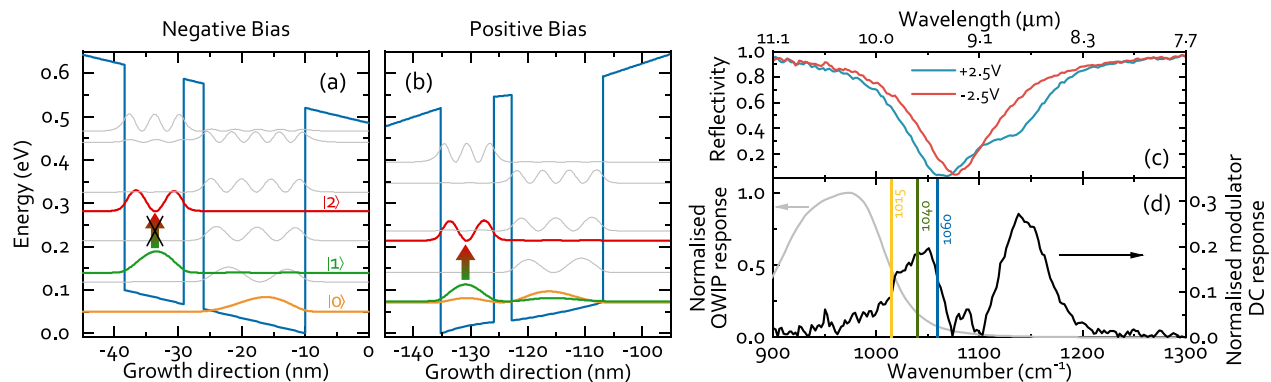
FIG. 2. (a) Calculated band structure (solid blue line), with squared modulus of the electronic wave-functions, of one period of the modulator AR at -2 V applied bias. The active transition $1 \rightarrow 2$ has a dipole of 2 nm, but the essentially depleted level $|1\rangle$ leads to operation in weak coupling when the structure is inserted in a patch cavity. (b) Calculated band structure at $+2$ V applied bias. Levels $|0\rangle$ and $|1\rangle$ are now aligned, electrons are delocalized and absorption takes place at the $1 \rightarrow 2$ transition energy (the splitting between levels $|0\rangle$ and $|1\rangle$ is smaller than the level linewidth). The band structures have been calculated with a home-written Schroedinger–Poisson solver that implements the model in Ref. 15. (c) DC reflectivity spectra of the modulator when applying -2.5 V/$+2.5$V DC potential difference (orange and light-blue curves, respectively). (d) Right axis: DC response of the modulator extracted from data in panel (c) following the definition in (2). Left axis: calculated fast QWIP responsivity curve (normalised) in gray (see Ref. 16).

dielectric constant of the QW material (InGaAs). Once in a MIM resonator, operation takes place in the strong coupling regime if the Rabi splitting $2\Omega_{Rabi} = \sqrt{f_w \omega_{pl}}$ is larger than the intersubband (ISB) and cavity linewidth (f_w is the overlap of the active QWs with the cavity electromagnetic mode, which can be approximated as the *total* thickness of the active QWs divided by the thickness of the active region).

The full modulators rely on MIM electrically connected patch resonators integrated with a coplanar waveguide for the RF operation [see the SEM image in Fig. 1(c)]. The details of the fabrication are described in the supplementary material, but a short description is given here. The heterostructure is first patterned (contact optical lithography) with a three-layered Ti-Au-Ti (5/200/20 nm) metal to implement the input coplanar RF-line (where wirebonding will take place), as well as the bottom continuous metal layer of the MIM cavities. A 35-nm-thick HfO$_2$ layer is inserted between the metallization and the AR to act as a gate (in future device generations it will be replaced by a thicker InGaAs cap layer). The sample is then epoxy-bonded to a SI-GaAs host substrate. The original InP substrate is removed in HCl until the InGaAs etch-stop is reached. The 435-nm-thick active region is now patterned on the bottom side and ready for further processing on the top side. 100 kV e-beam lithography is employed to define the patch structures and the 100-nm-wide connecting wires; Ti–Au (10/200 nm) is deposited as top contact and optical confinement layer; finally, the patch cavities are defined by ICP-RIE etching using the metal itself as a self-masking element. The last step of the process is the implementation of the air-bridge connections between the cavities and the RF central coplanar line, and it is described in the supplementary material. Wirebonding of the device to a PCB/SMA coplanar line completes the realization of the device.

Different devices have been fabricated by changing the length s of the patch cavities' side [see Fig. 1(a)] in the range 1.3–1.7 μm. The active region being very thin (435 nm), the system operates in the independent resonator regime; therefore, the cavity resonant fundamental frequency ν_{cav} can be tuned with s based on the following equation:[19,21]

$$\frac{c}{\nu_{cav}} = \lambda_{cav} = 2\,s\,n_{eff}. \quad (1)$$

A good choice of s for a modulator is such that $\nu_{cav} \approx \nu_{ISB}$, where ν_{ISB} is the frequency of the ISB transition. In this situation, the spectrum in strong coupling shows two polaritonic dips of equal amplitude, and the modulator response is the same at both frequencies. Of course, this is not a requirement, and a different choice can be justified by the application. The device reflectivities as a function of a DC applied bias have been probed with an infrared microscope connected with a Fourier transform infrared (FTIR) spectrometer. A typical result is reported in Fig. 2(c). The DC modulator contrast can be extracted from the data as

$$|R_{\min-bias} - R_{\max-bias}|, \quad (2)$$

where $R_{\min-bias(\max-bias)}$ is the reflectivity value at the minimum (maximum) applied bias on the modulator, respectively. From this first generation devices, we can expect a maximum modulation contrast in the 0.15–0.20 range.

From the device surface (composed of all the patch cavities, the electrical connections between the cavities, and the regions where the air-bridges land), we can estimate a capacitance of 0.37 pF. This leads to a cutoff frequency $f_{-3dB} = 1/(2\pi RC)$ of about 8 GHz, R being the

52.5 Ω value corresponding to the access circuit. As the device impedance is very high, ≥ 1 MΩ, and it is in parallel with the capacitance, it does not affect the cutoff. We have used an equivalent circuit, albeit simplified, to the one employed in Ref. 22 (see the supplementary material for details).

We have measured the electro-optic modulation bandwidth (BW) of the modulators with the setup described in the supplementary material (Fig. S1), which was also used in our previous work.[18] In particular—for the BW measurements—we have employed a home-made fast quantum well infrared photodetector (QWIP) based on the architecture presented in Ref. 22. Figure 2(d) (left axis) reports (gray solid line) the calculated spectral responsivity of the QWIP device we use, from Ref. 16. The modulator operates on the tail of the spectral responsivity curve of this type of detectors, which however exhibit a flat bandwidth up to more than 40 GHz at room temperature. Such speed is crucial to faithfully characterize the frequency response of the modulators.

Figure 3(a) reports the modulation amplitude vs frequency when the device is driven with 9 dBm RF input power and 24 mW incident laser CW power. The measurements have been acquired for different laser wavelengths [see solid vertical yellow, green, and blue lines in Fig. 2(d), namely: 9.85 μm (1015 cm^{-1}), 9.61 μm (1040 cm^{-1}), and 9.43 μm (1060 cm^{-1})]. The change in modulation amplitude with wavelength is mainly due to operation on the tail of the QWIP detector response curve.

The data [filled circles in Fig. 3(a)] can be fitted with a first-order low-bandpass curve (the fit function is $R(\nu) = R_0 + 20 \times \log_{10}\left(\frac{\nu_c}{\sqrt{\nu_c^2 + \nu^2}}\right)$, where ν_c is the -3 dB cut-off frequency) (solid lines), revealing that the devices operate up to 20 GHz (the limit of our spectrum analyzer). An average -3 dB cutoff at ≈ 8.2 GHz can be estimated at all the laser wavelengths (the dip at ≈ 1.5 GHz is a resonance in the detection chain that we did not manage to eliminate yet).

Figure 3(b) reports the BW at a laser wavelength of 9.85 μm for increasing RF input powers: 0, 3, 6, and 9 dBm. The measurements show that the modulator response is linear with the input power, and the BW keeps constant too. The inset of Fig. 3(b) shows the dependence of the modulator response on the incident laser power, up to 24 mW. The response is linear up to 15 mW. A beginning of saturation appears between 15 and 24 mW. This power is in accordance with the theory developed in Ref. 23 that suggests that low intensity saturation (I_{sat}) values of the order of several kW/cm^2 are possible in these first-generation devices operating close to the onset of the strong light–matter coupling regime. We have recently experimentally measured such low values while developing semiconductor saturable absorption mirrors (SESAM) in the mid-IR.[24] Furthermore, evidence of responsivity decrease with increasing incident optical power in fast QWIPs has been recently attributed to optical saturation as well.[16]

A binary data modulation signal has been applied to display eye diagrams as a figure of merit of the ultrafast modulators. To this scope, we employed a commercial fast MCT detector (VIGO Systems) delivering more signal voltage at the output compared to our fast QWIP that—as seen previously—operates on the tail of its responsivity curve [see Fig. 2(c), gray line]. The MCT detector used has a nominal bandwidth of 800 MHz, as detailed in the supplementary material, which limits the observable data rate. Figure 4 shows eye diagrams acquired with a pseudo-random binary sequence (PRBS) up to 1.5 Gbit/s. The
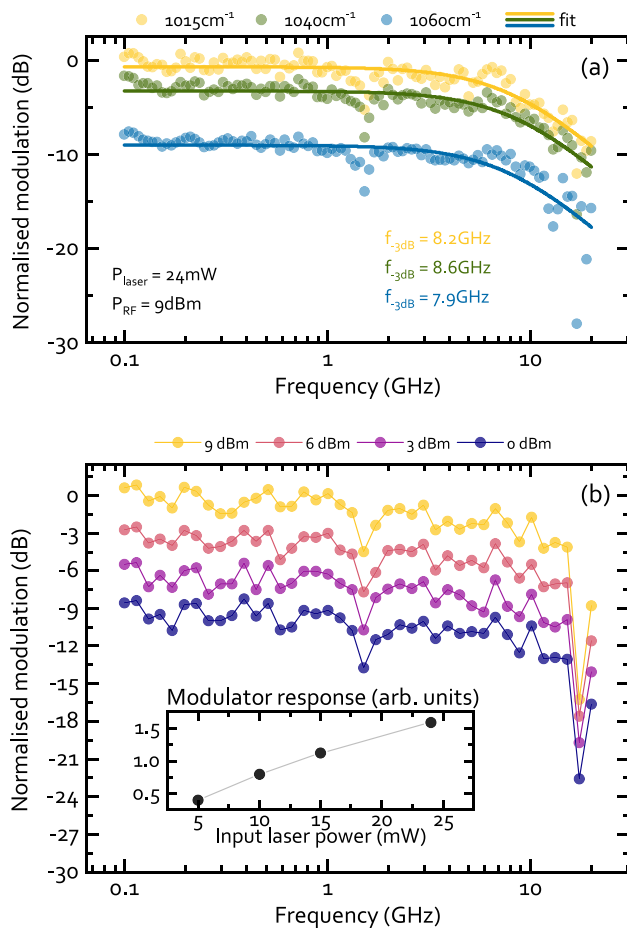
FIG. 3. (a) Modulator bandwidths (filled circles) measured at different laser wavelengths (CW power 24mW): 9.85 μm (1015 cm^{-1}), 9.61 μm (1040 cm^{-1}), and 9.43 μm (1060 cm^{-1}). Solid lines are data best-fits with a first-order low-bandpass curve: for each dataset, the f$_{-3dB}$ cutoff is reported too. The dip at 1.5 GHz is a resonance in the detection chain. (b) Modulator bandwidths for increasing RF input power: 0, 3, 6, and 9 dBm. The laser power and wavelength are 24 mW and 9.85 μm (1015 cm^{-1}), respectively. The modulator operation is linear with input RF power. Inset: modulation response as a function of the laser power. An initial onset of possible saturation is visible at 25 mW.

FIG. 4. Eye diagrams at (a) 1Gbit/s and (b) 1.5Gbit/s (limited by VIGO MCT bandwidth).

binary digit states of the numerical transmitted signal are defined, respectively, either with light transmission or light extinction. The high voltage level in the reported eye diagrams corresponds to the light transmission. The eye diagram exhibits a clear discrimination between low and high voltage levels and a wide time separation between the level transitions. The rise and fall times around 300 ps can be directly assigned to the 800 MHz-limited bandwidth of the detector characteristics. The modulator cutoff frequency effect being not visible on this display confirms that the cutoff frequency is well beyond the detector bandwidth.

In conclusion, we have exploited an electrically reconfigurable surface to demonstrate a free-space, room-temperature amplitude modulator for mid-infrared radiation with a −3 dB cutoff at about 8.2 GHz. The device operates in the 9.4–9.8 and 8.5–8.9 μm

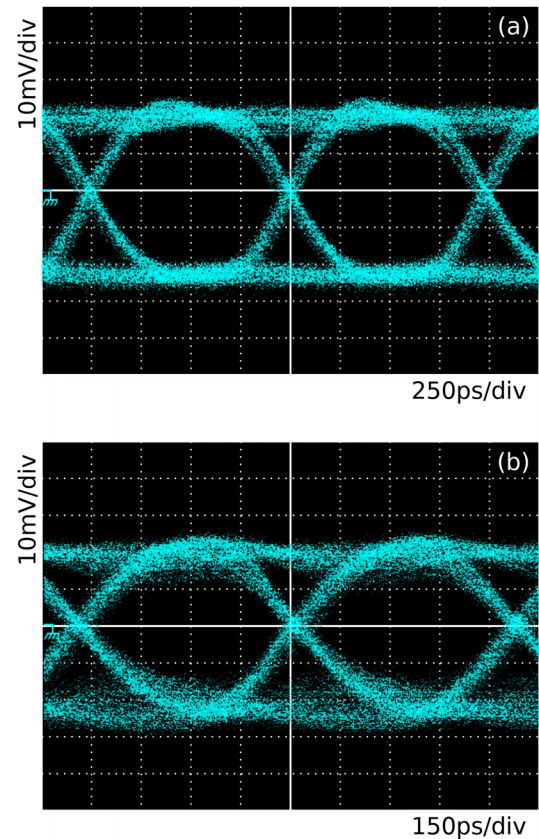wavelength range, with RF input powers up to 9 dBm. Future developments will focus on increasing the performance, in terms of modulation contrast, speed, and spectral response in order to make these devices compatible with spectroscopy (short-term) and phase-modulation[6] (long-term) applications. In particular, the speed can be increased by further reducing the device total surface (hence, reducing the capacitance). This can be obtained by further separating the patch resonators. Finally, we have recently developed an optical analogous of this system, where such transition is *optically* induced in order to implement SESAMs operating across the whole mid-IR.[23,24] A cross-breeding of these two approaches is also possible, i.e., devices whose nonlinear properties are tunable with an externally applied bias.

See the supplementary material for (i) details of the RF modulation measurement setup; (ii) BW of the fast, commercial MCT detector; (iii) device fabrication; (iv) AR details; and (v) S-parameters.

AUTHOR DECLARATIONS

Conflict of Interest

The authors have no conflicts to disclose.

Author Contributions

Mario Malerba and Stefano Pirotta contributed equally to this work.

Mario Malerba: Conceptualization (lead); Data curation (lead); Formal analysis (lead); Investigation (lead); Methodology (lead); Visualization (equal); Writing – review & editing (equal). **Stefano Barbieri:** Methodology (supporting); Writing – review & editing (supporting). **Guy Aubin:** Investigation (equal); Methodology (equal); Writing – review & editing (supporting). **L. Lucia:** Methodology (equal). **M. Jeannin:** Formal analysis (equal); Investigation (equal); Methodology (equal); Software (equal); Writing – review & editing (equal). **J.-M. Manceau:** Conceptualization (equal); Formal analysis (equal); Investigation (equal); Methodology (equal); Writing – review & editing (equal). **A. Bousseksou:** Conceptualization (equal); Formal analysis (equal); Investigation (equal); Methodology (equal); Writing – review & editing (equal). **Q. Lin:** Methodology (supporting). **J.-F. Lampin:** Methodology (supporting). **E. Peytavit:** Methodology (supporting). **S. Pirotta:** Conceptualization (equal); Data curation (equal); Formal analysis (lead); Investigation (equal); Methodology (lead); Software (lead); Visualization (equal); Writing – review & editing (equal). **L. H. Li:** Conceptualization (supporting); Investigation (supporting); Methodology (equal). **A. G. Davies:** Methodology (equal). **E. H. Linfield:** Investigation (supporting); Methodology (equal); Writing – review & editing (equal). **Raffaele Colombelli:** Conceptualization (lead); Data curation (lead); Formal analysis (lead); Funding acquisition (lead); Investigation (lead); Methodology (lead); Supervision (lead); Visualization (equal); Writing – original draft (lead); Writing – review & editing (equal).

DATA AVAILABILITY

The data that support the findings of this study are available from the corresponding authors upon reasonable request.

REFERENCES

[1] H.-T. Chen, J. F. O'Hara, A. K. Azad, A. J. Taylor, R. D. Averitt, D. B. Shrekenhamer, and W. J. Padilla, "Experimental demonstration of frequency-agile terahertz metamaterials," Nat. Photonics **2**, 295–298 (2008).

[2] L. Liu, L. Kang, T. S. Mayer, and D. H. Werner, "Hybrid metamaterials for electrically triggered multifunctional control," Nat. Commun. **7**, 13236 (2016).

[3] R. S. Ketchum and P.-A. Blanche, "Diffraction efficiency characteristics for MEMS-based phase-only spatial light modulator with nonlinear phase distribution," Photonics **8**, 62 (2021).

[4] J. Park, J. H. Kang, S. J. Kim, X. Liu, and M. L. Brongersma, "Dynamic reflection phase and polarization control in metasurfaces," Nano Lett. **17**, 407–413 (2017).

[5] I.-C. Benea-Chelmus, M. L. Meretska, D. L. Elder, M. Tamagnone, L. R. Dalton, and F. Capasso, "Electro-optic spatial light modulator from an engineered organic layer," Nat. Commun. **12**, 5928 (2021).

[6] H. Chung, I. Hwang, J. Yu, G. Boehm, M. A. Belkin, and J. Lee, "Electrical phase modulation based on mid–infrared intersubband polaritonic metasurfaces," Adv. Sci. **10**, 2207520 (2023).

[7] M. C. Sherrott, P. W. Hon, K. T. Fountaine, J. C. Garcia, S. M. Ponti, V. W. Brar, L. A. Sweatlock, and H. A. Atwater, "Experimental demonstration of >230° phase modulation in gate-tunable graphene-gold reconfigurable mid-infrared metasurfaces," Nano Lett. **17**, 3027–3034 (2017).

[8] V. Bernard, C. Daussy, G. Nogues, L. Constantin, P. Durand, A. Amy-Klein, A. Van Lerberghe, and C. Chardonnet, "CO_2 laser stabilization to 0.1-Hz level using external electrooptic modulation," IEEE J. Quantum Electron. **33**, 1282–1287 (1997).

[9] O. Spitz, P. Didier, L. Durupt, D. A. Diaz-Thomas, A. N. Baranov, L. Cerutti, and F. Grillot, "Free-space communication with directly modulated mid-infrared quantum cascade devices," IEEE J. Select. Top. Quantum Electron. **28**, 1200109 (2022).

[10] V. Berger, N. Vodjdani, D. Delacourt, and J. P. Schnell, "Room-temperature quantum well infrared modulator using a Schottky diode," Appl. Phys. Lett. **68**, 1904 (1996).

[11] E. Dupont, D. Delacourt, V. Berger, N. Vodjdani, and M. Papuchon, "Phase and amplitude modulation based on intersubband transitions in electron transfer double quantum wells," Appl. Phys. Lett. **62**, 1907–1909 (1993).

[12] E. Herrmann, H. Gao, Z. Huang, S. R. Sitaram, K. Ma, and X. Wang, "Modulators for mid-infrared and terahertz light," J. Appl. Phys. **128**(14), 140903 (2020).

[13] H. Dely, T. Bonazzi, O. Spitz, E. Rodriguez, D. Gacemi, Y. Todorov, K. Pantzas, G. Beaudoin, I. Sagnes, L. Li, A. G. Davies, E. H. Linfield, F. Grillot, A. Vasanelli, and C. Sirtori, "10 Gbit s^{-1} free space data transmission at 9 μm wavelength with unipolar quantum optoelectronics," Laser Photonics Rev. **16**, 2100414 (2022).

[14] T. H. N. Nguyen, V. Turpaud, N. Koompai, J. Peltier, S. Calcaterra, G. Isella, J. R. Coudevylle, C. Alonso-Ramos, L. Vivien, J. Frigerio, and D. Marris-Morini, "Integrated PIN modulator and photodetector operating in the mid-infrared range from 5.5 μm to 10 μm," Nanophotonics **13**, 1803–1811 (2024).

[15] C. Sirtori, F. Capasso, J. Faist, and S. Scandolo, "Nonparabolicity and a sum rule associated with bound-to-bound and bound-to-continuum intersubband transitions in quantum wells," Phys. Rev. B **50**, 8663–8674 (1994).

[16] Q. Lin, M. Hakl, S. Lepillet, H. Li, J.-F. Lampin, E. Peytavit, and S. Barbieri, "Real-time, chirped-pulse heterodyne detection at room temperature with 100 GHz 3-dB-bandwidth mid-infrared quantum-well photodetectors," Optica **10**, 1700 (2023).

[17] C. Balanis, *Antenna Theory: Analysis and Design* (Wiley-VCH Verlag GmbH, 2005), p. 1136.

[18] S. Pirotta, N.-L. Tran, A. Jollivet, G. Biasiol, P. Crozat, J.-M. Manceau, A. Bousseksou, and R. Colombelli, "Fast amplitude modulation up to 1.5 GHz of mid-IR free-space beams at room-temperature," Nat. Commun. **12**, 799 (2021).

[19] Y. Todorov, L. Tosetto, J. Teissier, A. M. Andrews, P. Klang, R. Colombelli, I. Sagnes, G. Strasser, and C. Sirtori, "Optical properties of metal-dielectric-metal microcavities in the THz frequency range," Opt. Express **18**, 13886 (2010).

[20] A. A. Anappara, A. Tredicucci, F. Beltram, G. Biasiol, and L. Sorba, "Tunnel-assisted manipulation of intersubband polaritons in asymmetric coupled quantum wells," Appl. Phys. Lett. **89**, 171109 (2006).

[21] C. Manolatou and F. Rana, "Subwavelength nanopatch cavities for semiconductor plasmon lasers," IEEE J. Quantum Electron. **44**, 435–447 (2008).

[22] M. Hakl, Q. Lin, S. Lepillet, M. Billet, J.-F. Lampin, S. Pirotta, R. Colombelli, W. Wan, J. C. Cao, H. Li, E. Peytavit, and S. Barbieri, "Ultrafast quantum-well photodetectors operating at 10 μm with a flat frequency response up to 70 GHz at room temperature," ACS Photonics **8**, 464–471 (2021).

[23] M. Jeannin, J.-M. Manceau, and R. Colombelli, "Unified description of saturation and bistability of intersubband transitions in the weak and strong light-matter coupling regimes," Phys. Rev. Lett. **127**, 187401 (2021).

[24] M. Jeannin, E. Cosentino, S. Pirotta, M. Malerba, G. Biasiol, J.-M. Manceau, and R. Colombelli, "Low intensity saturation of an ISB transition by a mid-IR quantum cascade laser," Appl. Phys. Lett. **122**(24), 241107 (2023).